Real-time imaging of enzymatic degradation of pretreated maize internodes reveals different cell types have different profiles

Amandine Leroy, M.F. Devaux, Mathieu Fanuel, Hugo Chauvet, Sylvie Durand, Camille Alvarado, Anouck Habrant, Christophe Sandt, Hélène Rogniaux, Gabriel Paës, et al.

Real-time imaging of enzymatic degradation of pretreated maize internodes reveals different cell types have different profiles

Amandine Leroy [1,5], Marie-Françoise Devaux [1], Mathieu Fanuel [1,2], Hugo Chauvet [3], Sylvie Durand [1], Camille Alvarado [1], Anouck Habrant [5], Christophe Sandt [4], Hélène Rogniaux [1,2], Gabriel Paës [5], Fabienne Guillon [1]*

[1] INRAE, UR 1268 BIA, 44316 Nantes, France

[2] INRAE, BIBS Facility, 44316 Nantes, France

[3] DISCO beamline, SOLEIL Synchrotron, BP48, l'Orme des Merisiers, 91192 Gif-sur-Yvette CEDEX, France

[4] SMIS beamline, SOLEIL Synchrotron, BP48, l'Orme des Merisiers, 91192 Gif-sur-Yvette CEDEX, France

[5] Université de Reims Champagne Ardenne, INRAE, FARE, UMR A614, 51100 Reims, France

* Corresponding author

Abstract

This work presents a dynamic view of the enzymatic degradation of maize cell walls, and sheds new light on the recalcitrance of hot water pretreated maize stem internodes. Infra-red microspectrometry, mass spectrometry, fluorescence recovery after photobleaching and fluorescence imaging were combined to investigate enzymatic hydrolysis at the cell scale. Depending on their polymer composition and organisation, cell types exhibits different extent and rate of enzymatic degradation. Enzymes act sequentially from the cell walls rich in accessible cellulose to the most recalcitrant cells. This phenomenon can be linked to the heterogeneous distribution of enzymes in the

liquid medium and the adsorption/desorption mechanisms that differ with the type of cell.

Keywords

Lignocellulose, Hot water pretreatment, Microspectrometry, Fluorescence, FTIR microspectroscopy.

1. Introduction

In recent decades, to reduce our dependence on fossil carbon resources, the world has been moving towards a sustainable economy based on the use of renewable resources, including lignocellulosic biomass (Chundawat et al., 2011; Wang et al., 2021). Among possible ways of transforming this biomass, enzymatic bioconversion is an appropriate strategy for the production of numerous biomolecules to be used in the chemistry and energy sectors (Bichot et al., 2018).

Interest in the use of agricultural residues as lignocellulosic resources is currently high (Vo et al., 2020). Maize is the main cereal grown in the world with an annual production of around 1,100 million tonnes and accounted for more than 38% of world cereal production in 2019 (FAOSTAT). Maize stems are among the most abundant crop residues produced every year. They are rich in cellulose (average 40.9%) (Bichot et al., 2018; Leroy et al., 2021), which makes them attractive for biorefineries (Arnaud et al., 2020; Leroy et al., 2021; Wang et al., 2021).

However, like other lignocellulosic biomass, the value of maize stems is limited by their intrinsic recalcitrance, which prevents efficient enzymatic degradation of cell wall polymers. Recalcitrance results from the combination of many multi-scale factors conferred by the close association of the cell wall constituents (cellulose, hemicelluloses and lignin) (Chundawat et al., 2011). At macroscopic scale, maize stems are made up of many cell types, differing mainly in the composition and physico-chemical properties of

49 their cell walls. (Barros-Rios et al., 2012; Berger et al., 2021; Devaux et al., 2018; El
50 Hage et al., 2018). At the microscopic scale, the relative amount cell wall polymers and
51 their chemical structure (degree of substitution of polysaccharides, lignin condensation,
52 cellulose crystallinity) contribute to biomass recalcitrance. They influence the
53 organisation and properties of the cell wall, which in turn, determine enzyme access to
54 their substrates (Zhao et al., 2012; Zoghlami & Paës, 2019).

55 In order to reduce lignocellulose recalcitrance, pretreatments, such as hot water
56 pretreatment (HWP), are carried out upstream of enzymatic hydrolysis. Previous
57 research has shown that HWP changes the composition of the cell wall with notably a
58 loss of hemicelluloses but also alters the structure of residual polymers through
59 condensation of lignin and an increase in the proportion of crystalline cellulose (Fan et
60 al., 2016; Leroy et al., 2021). At the molecular level, these changes have been shown to
61 alter the porosity of cell walls and thus to promote enzymatic hydrolysis (Leroy et al.,
62 2021). However, bioconversion is generally not complete, suggesting cell wall material
63 is still recalcitrant to enzymatic hydrolysis after HWP (Leroy et al., 2021; Li et al.,
64 2014).

65 In most studies, the effect of enzymatic pretreatment/hydrolysis on the properties
66 of lignocellulose was studied using whole biomass in powder form. However, as
67 mentioned above, the maize stem is composed of different types of cells with different
68 compositions and properties, which may react differently to pretreatments, resulting in
69 different sensitivity to enzymatic degradation (Arnaud et al., 2020; Barros-Rios et al.,
70 2012; Devaux et al., 2018; Ding et al., 2012; Donohoe et al., 2011; El Hage et al., 2018;
71 Nagle et al., 2020) and explaining the partial conversion of polysaccharides into
72 monosaccharides (Leroy et al., 2021). Examining the enzymatic degradation profile of

individual cell types in relation to the composition and properties of their cell wall could thus help identify the parameters involved in cell wall recalcitrance.

In addition to accounting for the heterogeneity of maize stem composition, the kinetics of the enzymatic reaction could also shed new light on the recalcitrance phenomenon (Chabbert et al., 2017; Devaux et al., 2018; Donaldson & Vaidya, 2017; Luterbacher et al., 2015). Devaux et al. (2018) showed that the type of cells in maize stem sections can be also differentiated based on the enzymatic degradation kinetics of their cell wall.

In this study, an experiment combining the kinetic aspect of the degradation and cell specificity was conducted. Maize stem internodes underwent hot water pretreatment (HWP). Changes in composition caused by the pretreatment as well as the kinetics of cell wall degradation of two cell types were monitored using synchrotron FTIR microspectroscopy and mass spectrometry imaging (MALDI-TOF). The location / adsorption of the enzymes as well as their mobility depending on the cell type were also monitored using the DISCO synchrotron beamline and florescence recovery after bleaching (FRAP) analyses, respectively. The result was a dynamic view of both the substrate and enzyme dynamics.

2. Material and methods

2.1 Plant material

The maize genotype F7025 was cultivated in INRAE experimental plots in Mauguio (South of France) under irrigated conditions and harvested at the silage stage. Internodes under the main ear were isolated, dried and cut into 2-cm fragments. The soluble components were removed from the fragment via 8-hour ethanol extraction followed by a 48-hour water extraction to recover the cell wall residue fragments.

2.1.1 Hot water pretreatment

Hot water pretreatment (HWP) was performed on half (i.e. 1-cm) fragments of cell wall residues in mineralization bombs equipped with Teflon cups (Parr, USA). Each half-fragment was pretreated with a volume of deionized water corresponding to a ratio of 1:30 (v/w) in an oil bath at 180 °C for 40 min (Herbaut et al., 2018a). The fragments were cooled in ice then washed with a 50:50 (v:v) ethanol: deionized water to remove the soluble components. HWP parameters were chosen based on the results of previous experiments to preserve the tissues organisation for microscopy imaging (Herbaut et al., 2018a; Leroy et al., 2021).

2.1.2 Sample preparation

All the fragments were embedded in polyethylene glycol and 20, 40 and 80 µm thickness sections were cut using a rotary Microm HM 360 Automated Microtome (Thermo Scientific, USA) for Fourier transform infrared (FTIR) microspectroscopy, deep UV fluorescence/ fluorescence recovery after photobleaching (FRAP) analysis, and matrix-assisted laser desorption/ionization-mass spectrometry (MALDI-MS) imaging, respectively. Successive washes with deionized water were performed to remove polyethylene glycol from the sections.

2.1.3 FASGA staining

FASGA staining was used on 80-µm-thin maize stem sections according to the method described previously by (El Hage et al., 2018). Images of the stained sections were acquired using fluorescence macroscope (AZ100 Multizoom microscope, Nikon, Japan).

2.2 Enzyme preparation

The commercial cellulase product Celluclast *1.5*, derived from *Trichoderma reesei* (*Novozymes* A/S, Bagsværd, *Denmark*), was used for cell wall enzymatic degradation. The commercial cellulase has a cellulase activity, xylanase activity and

protein loading of 77 FPU.mL^{-1}, 507 IU.mL^{-1} and 50.7 mg.mL^{-1}, respectively. The enzyme preparation was desalted on a PD10 column (GE Healthcare Bio-Sciences AB, Uppsala, Sweden). After desalting, the preparation has a cellulase activity of 21.9 FPU.mL^{-1}. It was applied on cross-sections at a dilution of 40 FPU.g^{-1} of biomass corresponding to a loading of 80 FPU.g^{-1} of glucan.

2.3 Synchrotron infrared imaging using a microfluidic device

2.3.1 Acquisition parameters and system settings

MID-infrared spectra were acquired on the SMIS beamline of the SOLEIL synchrotron using an FTIR microspectrophotometer coupled to the synchrotron source (Thermo Nicolet 5700 spectrometer combined with a Continuum XL microscope - Thermo Fisher Scientific, WI, USA) with the same acquisition parameters as described by (Devaux et al., 2018). Enzymatic degradation was performed on 20-µm cross sections using a microfluidic device as described by (Devaux et al., 2018). The whole cell volume was ~4 µl. The enzyme solution was then delivered at a constant flow rate of 2 µL.min^{-1}. The reaction was performed at 50 °C for approximately one hour. Spectra were acquired at 5-min intervals for selected points on parenchyma cell walls near the rind and in the pith. Enzymatic degradation of raw and pretreated samples were repeated 3 times.

2.3.2 Spectra analysis

The FTIR spectra were pretreated using homemade functions written in MATLAB (2020a) (Devaux et al., 2018). All the spectra were smoothed using a moving window of size 3. The region between 1,580–910 cm^{-1} was selected to compare the chemical composition of different types of cells. The baselines were corrected using linear segments with 3 points at 910, 1,190, and 1,580 cm^{-1}. Spectra at T=0 were normalized so that the area under the spectrum was equal to 1. The changes in

148 polysaccharide composition of the cell wall during degradation were studied in the
149 fingerprint region between 1,180–950 cm^{-1}. For a given point, time-lapse spectra were
150 normalized as follows: the maximum absorbance of the spectrum acquired at T=0 was
151 taken as normalization factor. All the time-lapse spectra acquired at this point were
152 divided by this maximum absorbance (Devaux et al., 2018). The change in the sum of
153 absorbance after normalization was used to compare the results of the different
154 experiments.

155 **2.4 Synchrotron deep- ultraviolet fluorescence imaging**

156 **2.4.1 Acquisition parameters**

157 Synchrotron fluorescence imaging was performed on the DISCO beamline of the
158 SOLEIL synchrotron using the Telemos microscope as described by (Devaux et al.,
159 2018). The excitation wavelength was set to 275 nm. A dichroic mirror at 300 nm
160 (Omega Optical Inc., USA) and two emission bandpass filters were used for
161 multispectral image acquisition: a 327–353 nm filter (Semrock, Rochester, USA) to
162 locate enzymes without labelling, thanks to the autofluorescence of tryptophan and
163 tyrosine amino acids; and a 420–480 nm filter (Semrock, Rochester, USA) to image cell
164 walls using the autofluorescence of phenolic compounds. The samples were observed
165 with a 10× (NA 0.2) Ultrafluar Zeiss objective (Carl Zeiss GmbH, Germany), which
166 provides fields of view of 1,116 × 1,116 μm^2 with pixel sizes of 1.092 µm. The
167 acquisition time was set at 30 s and 6 s for the emission filters 327–353 and 420–480
168 nm, respectively.

169 A 0.5 × 0.5 cm square section (thickness 40 µm) was placed on a quartz slide
170 (Circular-Qtz 25.0 ref. R525000, Esco optics, NJ 07438, USA) fitted with a 1 × 1 cm
171 spacer (thickness 0.25 mm) (ref AB0576 Gene Frame R, Thermo Scientific, France).
172 Enzyme solution (30 µL), with the same quantity of buffer used for the controls, was

added on the cross-section, and the system was then sealed with a second quartz slide. During the hydrolysis reaction, the sample was maintained at a temperature of 50 °C using a heating chamber. Acquisitions were made at 4-min intervals during the 92 min of hydrolysis. Three experiments were performed on raw and pretreated sections using enzyme and 2 experiments using buffer. Each section allowed the degradation of the rind and pith parenchyma to be monitored in the same experiment.

2.4.2 Image analysis

All the fluorescence images were pre-processed as described by (Vidot et al., 2019). The enzyme and the cell wall fluorescence images were combined for viewing to obtain RGB images, with the enzyme image set to the red and green channels and the cell wall image set to the blue channel. Movies were made of the images acquired over time to monitor cell wall degradation, and the distribution of the enzyme during enzymatic degradation. The fluorescence intensities were measured to quantify the relative amount of enzymes found on cell walls and in cell lumen of both the rind and pith parenchyma. For each pretreatment condition (raw and HWP sections) and cell type, 3 segments of cell wall and 3 regions corresponding to the cell lumens were manually selected. For each pretreatment condition and cell type, the average fluorescence intensities on the cell wall and in the lumen were determined over time throughout the experiment, i.e. 9 measurements (3 segments x 3 experiments). The fluorescence profiles as well as the analysis of variance were carried out using homemade MATLAB (2020a) functions (Devaux et al., 2018).

2.5 Matrix-Assisted Laser Desorption/Ionization-Mass Spectrometry Imaging

2.5.1 Preparation and in-situ enzymatic hydrolysis of sections

Sections (thickness 80 µm) were deposited on indium tin oxide glass slides (Bruker, Germany ref. 8237001) covered with adhesive carbon tape (Agar Scientific,

198 ref. AGG3939B). A solution was prepared of Celluclast® filtered through an Amicon
199 Ultra Centrifugal filter MWCO 10 kDa (UFC501008) and with a cellulase activity of
200 26.6 FPU.mL^{-1}. The enzyme solution was deposited by nebulisation using a homemade
201 robot (Veličković et al., 2014). The slides were then incubated at 50 °C for different
202 periods: 0 min, 30 min, 90 min and 24 hours. For each condition, hydrolysis was
203 performed in duplicate.

204 **2.5.2 Mass spectrometry matrix and internal standard deposition**

205 A DMA/DHB matrix (100 mg.mL^{-1} DHB in 50:50 deionized water/acetonitrile,
206 2% DMA) was prepared as described by (Ropartz et al., 2011). To compensate for
207 tissue heterogeneity, an internal standard, pentaacetyl-chitopentaose (Megazyme,
208 Ireland) at 20 µg.mL^{-1}, was added to the matrix solution. A thin layer of the mixture (85
209 nL.mm^{-2}) was nebulised using an in-house-designed robot (Veličković et al., 2014).

210 **2.5.3 Acquisition and processing of mass spectrometry images**

211 Matrix-Assisted Laser Desorption/Ionization-Mass Spectrometry (MALDI MS)
212 analyses were acquired with a rapifleX MALDI Tissuetyper MALDI-TOF mass
213 spectrometer (Bruker, Bremen, Germany) with the same acquisition parameters as
214 described by (Arnaud et al., 2020). Acquired MS images were processed with
215 FlexImaging 5.0 software. Individual spectra were normalized to the area of the
216 pentaacetyl-chitopentaose peak to account for tissue heterogeneity and to improve the
217 view of the distribution of the released oligosaccharides. The images were coloured
218 according to the "flexImaging" colour scale, ranging from black (lowest intensity) to
219 white (highest intensity). The intensity scale was set using the same intensity values for
220 all the images in order to compare the abundance of the species.

221 **2.6 Fluorescence Recovery After Photobleaching**

222 **2.6.1 Sample preparation**

Square sections (diameter 0.5 × 0.5 cm, thickness 40 µm) were incubated overnight at room temperature in 0.01 mM of Dextran-rhodamine 40 kDa (DR40) (Sigma-Aldrich, ref. 42874). The hydrodynamic radii of DR40 and the cellulase enzymes in the Celluclast cocktail were determined using the same method as described by (Herbaut et al., 2018b). Sections were then mounted in the probe solutions between the slide and cover slip and sealed with polish for microscopy analysis.

2.6.2 Acquisition and analysis parameters

Fluorescence Recovery After Photobleaching (FRAP) analyses were performed with a Leica TCS SP8 confocal microscope (Leica Microsystems, Germany) using a 63 x oil-immersion objective (NA 1.4) and the same set-up and acquisition parameters as described by (Herbaut et al., 2018b; Paës et al., 2017). The parameters of the four acquisition phases were adapted for a total recovery measurement of approximatively 10 min as follows: 1-Pre-bleaching: 10 scans every 0.051 s with the 552 nm laser line set to a power of 2% of the maximum laser power; 2-Bleaching: 20 scans every 0.051 s with both 488 nm and 552 nm laser lines at 100% of power; 3- Post-bleaching: 200 scans, separated by 0.051 s, with the 552 nm laser line set to 2%, then 300 scans separated by 2 s, with the 552 nm laser line set to 2%. The diffusion coefficient of DR40 was identified using the method described by (Herbaut et al., 2018b).

3. Results and discussion

3.1 Variability of chemical composition according to the type of cell and the effect of the hot water treatment

FASGA staining was used to reveal the difference in the chemical composition of tissues in the raw and pretreated samples. FASGA staining makes it possible to distinguish highly lignified tissues, coloured red, and low-lignified and cellulose-rich tissues, coloured blue (El Hage et al., 2018; El Hage et al., 2021).

248 The majority of the tissues constituting the raw samples stained red, showing
249 that these tissues were lignified, as already reported for the same genotype (El Hage et
250 al., 2018) (Fig. 1 A). However, some regions, clearly visible in the enlargements,
251 stained blue, including the parenchyma under the rind (RP). The staining of these cell
252 types by Alcian Blue suggests that lignification of the cell walls was changed. After
253 HWP, the proportion of cell walls stained red was lower (Fig. 1B). Indeed, the pith
254 parenchyma between the vascular bundles (PP), stained red on the native sections, but
255 appeared blue in some areas after pretreatment. The PP parts that were still red after
256 HWP were denoted PP1. The PP parts that coloured blue after HWP were denoted PP2.
257 These observations suggest that HWP causes some changes in the chemical composition
258 or in the distribution of the cell wall polymers according to different cell types.
259 Two parenchyma, RP and PP, were chosen, and examined the differences in
260 composition between the two cell types and the changes induced by pretreatment in
261 more detail using FTIR microspectroscopy.
262 Comparing the average FTIR spectra of the two parenchyma in the raw sample
263 revealed differences in their chemical composition (Fig. 1C). The band at 1,510 cm^{-1},
264 characteristic of the aromatic C=C stretch of lignin (Gierlinger et al., 2008), showed
265 higher PP absorbance than RP. Both RP and PP spectra exhibited strong absorption
266 bands for polysaccharides between 1,200 and 950 cm^{-1} with a broad carbohydrate band
267 at 1,035–1,051 cm^{-1} and partly resolved bands at 1,160, 1,110, 1,000–995 cm^{-1}
268 (Gorzsás et al., 2011; Robert et al., 2005). This pattern in the spectral sugar fingerprint
269 region indicated a mixture of hemicellulosic sugars, which in maize, are mainly
270 glucoarabinoxylans (GAX), and cellulosic polysaccharides in varying proportions
271 depending on the type of cell. In the region between 1,180 and 920 cm^{-1}, in contrast to
272 PP, RP showed a stretch towards 1,030 cm^{-1}, corresponding to the C–O stretching signal

273 of β-(1-4) glucans (Robert et al., 2005). Interestingly, a substantial difference was
274 visible on the band at 1,250 cm^{-1}, characteristic of the C-O stretch of phenolics and
275 asymmetric C-C-O stretching of non-conjugated polysaccharide esters (Vermerris et al.,
276 2002), with cell walls showing higher PP absorbance than RP.

277 After HWP, two bands at 1,053 and 1,034 cm^{-1}, characteristic of cellulose, were
278 clearly distinguishable in both parenchyma (Fig. 1D) (Leroy et al., 2021). Like in the
279 raw parenchyma, at 1,250 cm^{-1} the absorbance of PPs was higher than of RP. Two
280 groups were distinguishable within PP (PP1 and PP2). In both PP groups, the proportion
281 of cellulose increased, and absorbances at 1,510 cm^{-1} were close. A significant decrease
282 in the band at 1,250 cm^{-1} was only observed in PP2.

283 These results revealed the contrasted chemical composition of the two raw
284 parenchyma. RP was rich in cellulose while PP was rich in lignin and in acetylated
285 GAX. The lignocellulosic biomass of maize is characterised by the presence of
286 hydroxycinnamic acids, mainly *p*-coumaric acid, ester-linked to the syringyl units of the
287 lignin, and ferulic acid, the latter acting as crosslinker between GAXs and between
288 GAX and lignin (Scheller & Ulvskov, 2010). It can therefore assume that the higher
289 absorbance of PP observed at 1,250 cm^{-1} is mainly due to the presence of
290 hydroxycinnamic acids and acetyl groups, linked by ester bonds to cell wall polymers.
291 The differences in cell wall composition of the two parenchyma revealed by FTIR
292 support the results of FASGA staining and are in agreement with previous FTIR
293 analyses of the same cell types of another maize stem genotype (Devaux et al., 2018).

294 In both RP and PP parenchyma, HWP induced relative cellulose enrichment as a
295 result of the loss of hemicelluloses (Batista et al., 2019; Leroy et al., 2021; Zeng et al.,
296 2012). Absorbance at 1,250 cm^{-1} decreased after HWP in RP and PP2, suggesting
297 removal of hydroxycinnamic acids and acetyl groups. Indeed during HWP, the

298 hydronium ions and organic acids produced by auto-ionization of water and the release
299 of organic acids (acetic acid) and uronic acids, trigger hydrolysis of hydroxycinnamic
300 acid linkages and of the GAX backbone (Fan et al., 2016).

301 To sum up FASGA and FTIR analysis of the chemical composition of the
302 samples highlighted the contrasted chemical composition of RP and PP cell types. In
303 general, HWP led to relative enrichment of cellulose in the two parenchyma through the
304 loss of GAX.

305 **3.2 Variability of the effect of pretreatment on enzymatic degradation**

306 **3.2.1 Monitoring variations in the chemical composition of tissues during**
307 **enzymatic hydrolysis**

308 Microfluidic FTIR microspectroscopy was used to monitor cell wall degradation
309 in real time and to examine the influence of the pretreatment. The degradation kinetics
310 was evaluated by monitoring the sum of absorbance of the sugar fingerprint spectral
311 region between 1,180 and 920 cm^{-1} using the sum of absorbances at all wavenumbers
312 and is shown for all experiments (Fig. 2).

313 Contrasted variations in the sum of the absorbance between RP and PP in the
314 raw samples during hydrolysis were observed (Fig. 2A). Progressive and almost
315 complete degradation of RP was observed after 1 hour of enzymatic degradation
316 whereas only a slight decrease was observed in the PP.

317 In the pretreated samples, different behaviours were observed in the pith
318 parenchyma (Fig. 2B, PP1 and PP2)). Two groups could be distinguished by their
319 kinetics. The first group, PP1, showed similar degradation profiles to those measured in
320 the raw PP with almost no change over time. In contrast, the second group of spectra,
321 PP2, showed a progressive decrease in absorbance in the sugar fingerprint region. Like
322 with raw RP, a progressive decrease in the absorbance in the sugar fingerprint region

was measured in pretreated RP (Fig. 2B). However, this decrease seemed to occur in three stages: a slow decrease between 0 and 15 min, a rapid decrease between 15 and 35 min, and a plateau after 35 min. The enzymatic degradation of the RP after pretreatment was faster and almost complete after 35 min.

As expected, rind and pith parenchyma showed contrasting enzymatic degradation consistent with the degradation profiles observed in other maize genotypes (Devaux et al., 2018; Jung & Casler, 2006; Lam et al., 2013). These profiles can be linked to their different chemical compositions. Indeed, the cell walls of RP were weakly lignified and easily degraded. The cell walls of PP cells, which were richer in lignin and ester bonds, remained almost intact during enzymatic hydrolysis. This difference in enzymatic degradation between the two cell types suggests that high concentrations of lignin and hydroxycinnamic acids in the cell wall affect the enzyme accessibility to the cellulose, as supported by over works (dos Santos et al., 2019; Grabber et al., 1998; Lam et al., 2003; Siqueira et al., 2011; Yoo et al., 2020; Zoghlami & Paës, 2019).

In the present study, the pretreatment increased the degradation capacity of RP and of some PP cell walls. The increase in the speed and efficiency of RP hydrolysis could be linked to the loss of hemicelluloses and associated ester linked hydroxycinnamic acids, which could facilitate access to cellulose by enzymes. Like lignin, hemicelluloses act as a protective barrier around cellulose due to their cross-linking with each other and with lignin via diferulic bridges, and their interaction with cellulose via hydrogen bonds (Meng & Ragauskas, 2014; Simmons et al., 2016). In the present study, HWP reduced the recalcitrance of PP but not homogeneously, and PP2 was more degraded than PP1. This contrasted degradation could be linked to a difference in the relative proportions of cellulose/lignin/ester bonds.

3.2.2 Tracking cellulose degradation products during the enzymatic hydrolysis

MALDI-MS imaging analyses were performed to monitor the degradation of cellulose in space according to the cell types, and to the pretreatment, through the mass detection of its degradation products, cello-oligosaccharides with a degree of polymerization (DP) of 2 to 4 (COS2 to COS4) and glucose, and their variations during enzymatic hydrolysis (Fig. 3).

During the degradation of the raw cell walls, COS were only detected in the RP; no COS were detected in the PP (Fig. 3A). After 30 min of hydrolysis, a high intensity COS4 signal was detected in the RP, showing that COS4 was the main product released at the beginning of cell wall hydrolysis (Fig. 3B). The signals observed for COS2 and COS3 were lower. A significant loss (80%) in the signal intensity of COS4 was measured after 90 min of hydrolysis, whereas the intensity of COS2 more than doubled (+ 126%) (Fig. 3C). These results suggest that between 30 and 90 min, COSs were converted to lower mass products. After 24 h, COS4 and COS3 signals were lower than the control intensities at 0 min and only a weak COS2 signal was measured, showing that most of the degradation occurs rapidly and suggesting that the majority of higher DP oligosaccharides were converted into lower molecular weight products over time. It was not possible to measure the glucose unit in the raw sections due to the presence of an undefined peak with a mass close to that of the expected glucose (m/z 203.2, $[M+Na]^+$ ionic species).

In contrast to the raw samples, the location of COSs between the different cell types in the pretreated samples was more diffuse (Fig. 3D). Indeed, COSs were detected in the RP and also in the PP. Looking more specifically at changes in the location of COS2 during hydrolysis, it was noted that at 30 min, COS2 was mainly located in RP, while at 90 min, it was located in PP near the centre of the internode. After 24 h, COS2

373 was only observed in the PP closest to RP. When looking at the COSs released on the
374 course of the enzymatic reaction, at the beginning of the reaction, no COS4 signal and
375 only a low intensity COS3 signal were detected (Fig. 3F). The main oligosaccharide
376 released after 30 min of hydrolysis was COS2. A progressive rise in COS3 and COS2
377 intensities occurred over the period of hydrolysis with maximum intensity reached after
378 90 min. The marked drop in the intensity of COS3 after 24 hours suggests its
379 conversion into lower DP between 90 minutes and 24 hours of hydrolysis (Fig. 3E). In
380 contrast to the raw sections, a high abundance of COS2 and glucose was measured after
381 24 hours.
382 The presence of COS2 as the main reaction product in the HWP section compared to
383 COS4 in the raw sections, suggests that the pretreatment favours the action/synergy of
384 the cellulolytic enzymes present in the enzyme cocktail, promoting the formation of
385 COSs with small DPs.
386 Tracking the distribution and relative abundance of COSs during hydrolysis
387 supports the previous observations. Indeed, in raw samples, COSs were only detected in
388 RP, showing that cellulose-rich and low-lignified tissues were degraded, confirming
389 previous FTIR analyses and in agreement with research on other genotypes (Arnaud et
390 al., 2020; Devaux et al., 2018). The production and distribution of COSs in the
391 pretreated section show that the hydrolysis was more complete than that of the raw
392 samples. However, in the pith region the efficiency of HWP was not consistent across
393 the section and appeared to vary with distance from the rind region. As the matter of
394 fact, the pretreatment appears more effective in the region that is in direct contact with
395 water. Furthermore, the difference in COSs distribution during the reaction across the
396 regions of the section suggests variations in degradation kinetics over time depending

on the type of cell concerned, which could be related to cell wall composition and hence to the efficiency of the HWP.

3.3 Location and mobility of the enzymes according to cell type

3.3.1 Monitoring enzyme distribution during hydrolysis

One of the hypotheses to explain the different degradation profiles of the two types of parenchyma cells is the heterogeneous distribution of enzymes. To test this hypothesis, the distribution of the enzymes during enzymatic hydrolysis using their autofluorescence properties under deep UV excitation was monitored (Fig. 4).

At the beginning of the reaction, raw and HWP sections showed contrasted location/intensity of enzyme fluorescence: no enzyme signal was detected in the raw RP (Fig. 4A), whereas a strong signal was observed in the pretreated RP (Fig. 4B). Enzyme fluorescence decreased over time in both cases. The differences between raw and pretreated RP were analysed more precisely by quantifying variations in enzyme fluorescence on the cell walls (Fig. 4C). At the start of hydrolysis, the fluorescence intensity on the walls of pretreated cells was higher than that measured on the walls of raw cells. Next, an increase in the intensity of enzyme fluorescence was observed until a maximum was reached in the raw samples at 19 min and in the pretreated samples at 12 min. This was followed by a slow decrease in the raw sample and a more rapid decrease in the pretreated sample until the end of the reaction. The enzyme fluorescence intensity measured at the centre of the cell lumens showed opposite variations to those measured on the cell walls (Fig. 4D): a slight decrease in enzyme fluorescence intensity was measured in RP lumens up to 16 min, followed by an increase.

These variations in enzyme fluorescence intensity suggest adsorption/desorption of the enzymes on the cell walls. Enzyme adsorption would explain the decrease in enzyme fluorescence in the lumens, and conversely, an increase in the cell walls. After

422 degradation of the cell wall polymers, enzymes would be released in the lumen,
423 explaining the increase in the fluorescence signal. The difference in enzyme intensity
424 and in the time at which maximum intensity was reached on the cell walls in raw and
425 pretreated sections showed that pretreatment promoted a rapid adsorption of enzymes,
426 thereby accelerating hydrolysis of the cell walls. The slow decrease in enzymes on raw
427 RP cell walls indicated that enzyme desorption was incomplete and that some enzymes
428 were retained in the cell walls: this could be linked to non-specific adsorption on cell
429 wall components (dos Santos et al., 2019; Yang & Pan, 2016), to a reduction in the
430 enzyme degradation capacity caused by more recalcitrant structures, or to inactivation
431 of the enzymes following prolonged exposure to UV.

432 In contrast to RP, no enzyme fluorescence was detected in the PP cell wall in
433 either the raw (Fig. 5A) or pretreated (Fig. 5B) sections, regardless of the duration of
434 hydrolysis. These observations were supported by the measurement of the enzyme
435 fluorescence intensity in the cell walls (Fig. 5C) and lumens (Fig. 5D): no variation in
436 the raw PP was detected during the reaction, whereas a progressive decrease in the
437 enzyme fluorescence intensity was measured on the cell walls and in the lumens in the
438 pretreated PP. Interestingly, within a small target area in the pretreated PP, weak
439 enzyme fluorescence was detected on the cell wall of one cell (Fig. 5B). By measuring
440 the variation in enzyme fluorescence intensity on this cell wall and within its lumen,
441 profiles close to those of the fluorescence variation of the enzymes in RP cells were
442 observed (see supplementary material).

443 The absence of fluorescence on the entire raw PP suggest that the enzymes were
444 not adsorbed on the cell walls. As the interaction of enzymes with substrates is a
445 necessary step for hydrolysis, the non-adsorption of the enzymes likely explains the
446 absence of degradation detected by FTIR or MALDI-MS. Like previous observations,

447 the location of the enzymes also highlighted the heterogeneity of the PP after
448 pretreatment. PP1, whose degradation was similar to that of the raw PP, showed no
449 adsorption of enzymes on the cell walls. Unfortunately, in the regions selected for UV
450 imaging PP2 with the exception of one cell was not present.

451 Even though no change in signal intensity or in enzyme adsorption over time
452 was observed in almost all pretreated PP, a decrease in enzyme fluorescence intensity
453 was measured in the lumens (Fig. 5D). These decreases in enzymes fluorescence
454 intensities could thus be linked to a lower concentration of enzymes in the PP medium
455 and suggest that the enzymes were distributed differently throughout the section
456 depending on the cell types and on pretreatment.

457 To investigate this hypothesis and to visualise the impact of pretreatment and
458 cell type on the distribution of enzymes in the medium at the beginning and the end of
459 the reaction, an analysis of the variance of fluctuations in the intensity of enzyme
460 fluorescence measured in the lumen was performed (Fig. 6). Fig. 6 shows the
461 distribution of the average intensities measured between 0 and 15 min or between 80
462 min and the end of the hydrolysis in each experiment.

463 During the first 15 minutes of the reaction, the spread of data indicates that both
464 pretreatment and the type of cell had an effect on the distribution of the enzymes in the
465 medium. In contrast, after 80 min (when reactions were considered as stabilised in raw
466 and pretreated parenchyma), only pretreatment (high F-value) had an effect on enzyme
467 distribution.

468 These results confirmed previous hypothesis that, at the beginning of the
469 reaction, the enzymes contained in the medium were concentrated in the easily
470 deconstructed tissues, the RP and in particular in the pretreated tissues. This movement
471 of the enzymes towards RP could explain the decrease in fluorescence intensity of the

enzymes in the lumens of the PP cells at the beginning of the reaction (Fig. 5D). After degradation of the RP, towards the end of the hydrolysis, the enzymes that were desorbed from the RP cell walls would be redistributed homogeneously throughout the medium. Redistribution of the enzymes would explain the increase in enzyme intensity in the lumens of the RP (Fig. 4D) as well as the slight increase observed in the PP (Fig. 5D). In parallel, the effect of pretreatment on the distribution of enzymes at the end of the reaction (Fig. 6) also suggests that HWP allows the adsorption of the enzymes on other areas of the PP or on cell types not observed in the present study.

The change in the location of the enzymes over time revealed not only the adsorption/desorption of the enzymes at the level of the cell walls, but also the capacity of the enzymes to migrate towards easily deconstructed cell types.

3.3.2 Estimation of cell wall accessibility through the diffusion of fluorescent probe

In order to understand the impact of HWP and cell type on the adsorption of enzymes by the cell wall, fluorescence recovery after photobleaching (FRAP) analyses were performed. For this purpose, the DR40 was selected based on intrinsic properties as being a neutral probe (no specific affinity for the components of the cell wall) and as having a hydrodynamic radius (3.8 nm) in the same range as cellulases (around 3.4 nm) (Bubner et al., 2012). DR40 has already been used to investigate the accessibility and steric hindrance of cell walls through the analysis of its diffusion (Herbaut et al., 2018b; Paës et al., 2017).

When the two raw parenchyma were compared, the diffusion coefficient of RP was significantly higher than that of PP. This shows that the probe diffused more easily in RP than in the PP. Following pretreatment, diffusion of DR40 did not change in RP. Two groups of PP, differing in their DR40 diffusion coefficient, were identified after

pretreatment. One of these groups was PP1, which behaved similarly to raw PP, while the second, PP2, had a higher diffusion coefficient than raw PP.

The difference in DR40 diffusion measured for PP and RP can be attributed to differences in cell wall composition. Compositional analyses (FASGA and FTIR) showed that PP was richer in lignin and ester bonds than RP. Both strongly limit access to cellulose by influencing cell wall porosity (Chundawat et al., 2011; Leroy et al., 2021; Li et al., 2018), which accounts for over 90% of the accessibility of hydrolytic enzymes inside the cell wall (Wang et al., 2012). The presence of a lower steric hindrance environment in the RP, with fewer lignin and ester bonds, is hypothesised to favour the diffusion, adsorption and subsequent hydrolysis by the enzyme, in agreement with the adsorption and degradation capacity of this type of cell observed by fluorescence and MALDI-MS/FTIR, respectively, and in agreement with the results of other studies (Devaux et al., 2018; Ding et al., 2012). Similarly, the changes that occurred in pretreated PP2 compared to pretreated PP1 and native PP, with the decrease in ester bonds and hemicellulose content (Fig. 1E), are hypothesised to favour diffusion of the probe. The changes would also explain the preferential location of enzymes and the degradation of the cell wall observed by FTIR. These results confirmed the fact that, in pretreated samples, the decrease in ester bonds and hemicellulose content, in the absence of any change in lignin content, increase the accessibility and degradation of pretreated cell walls.

4. Conclusion

The multimodal approaches makes it possible to relate variations in chemical composition (FTIR analyses) to accessibility of cell wall polymers to enzymes (FRAP), and location/adsorption of the enzymes (enzyme fluorescence), which provide keys to understand the different patterns of cell wall degradation according to cell type and

pretreatment. This multimodal approach could be advantageously applied to other biomass/pretreatment couples to further investigate recalcitrance. Regarding enzymes, it could help to further understand the synergetic actions between hydrolases and oxidative enzymes such as lytic polysaccharide monooxygenases, for which action mode is still partly unknown.

E-supplementary data for this work can be found in e-version of this paper online.

Acknowledgments

A. Leroy's PhD was funded by *Région Grand-Est* and *Grand Reims*.

References

1. Arnaud, B., Durand, S., Fanuel, M., Guillon, F., Méchin, V., Rogniaux, H., 2020. Imaging Study by Mass Spectrometry of the Spatial Variation of Cellulose and Hemicellulose Structures in Corn Stalks. J. Agric. Food Chem., 68(13), 4042-4050.

2. Barros-Rios, J., Santiago, R., Malvar, R.A., Jung, H.-J.G., 2012. Chemical composition and cell wall polysaccharide degradability of pith and rind tissues from mature maize internodes. Anim. Feed Sci. Technol., 172(3), 226-236.

3. Batista, G., Souza, R.B.A., Pratto, B., dos Santos-Rocha, M.S.R., Cruz, A.J.G., 2019. Effect of severity factor on the hydrothermal pretreatment of sugarcane straw. Bioresour. Technol., 275, 321-327.

4. Berger, M., Devaux, M.-F., Legland, D., Barron, C., Delord, B., Guillon, F., 2021. Darkfield and Fluorescence Macrovision of a Series of Large Images to Assess Anatomical and Chemical Tissue Variability in Whole Cross-Sections of Maize Stems. Front. Plant Sci., 12(3031).

5. Bichot, A., Delgenès, J.-P., Méchin, V., Carrère, H., Bernet, N., García-Bernet, D., 2018. Understanding biomass recalcitrance in grasses for their efficient utilization as biorefinery feedstock. Rev. Environ. Sci. Biotechnol., 17(4), 707-748.

546 6. Bubner, P., Dohr, J., Plank, H., Mayrhofer, C., Nidetzky, B., 2012. Cellulases dig
547 deep: in situ observation of the mesoscopic structural dynamics of enzymatic cellulose
548 degradation. J. Biol. Chem., 287(4), 2759-2765.
549 7. Chabbert, B., Habrant, A., Herbaut, M., Foulon, L., Aguié-Béghin, V., Garajova, S.,
550 Grisel, S., Bennati-Granier, C., Gimbert-Herpoël, I., Jamme, F., Réfrégiers, M., Sandt,
551 C., Berrin, J.-G., Paës, G., 2017. Action of lytic polysaccharide monooxygenase on
552 plant tissue is governed by cellular type. Sci. Rep., 7(1), 17792.
553 8. Chundawat, S., Donohoe, B., Sousa, L., Elder, T., Agarwal, U., Lu, F., Ralph, J.,
554 Himmel, M., Balan, V., Dale, B., 2011. Multi-scale visualization and characterization of
555 lignocellulosic plant cell wall deconstruction during thermochemical pretreatment.
556 Energy Environ. Sci., 4, 973-984.
557 9. Devaux, M.F., Jamme, F., Andre, W., Bouchet, B., Alvarado, C., Durand, S., Robert,
558 P., Saulnier, L., Bonnin, E., Guillon, F., 2018. Synchrotron Time-Lapse Imaging of
559 Lignocellulosic Biomass Hydrolysis: Tracking Enzyme Localization by Protein
560 Autofluorescence and Biochemical Modification of Cell Walls by Microfluidic Infrared
561 Microspectroscopy. Front Plant Sci, 9, 200.
562 10. Ding, S.-Y., Liu, Y.-S., Zeng, Y., Himmel, M.E., Baker, J.O., Bayer, E.A., 2012.
563 How Does Plant Cell Wall Nanoscale Architecture Correlate with Enzymatic
564 Digestibility? Science, 338(6110), 1055-1060.
565 11. Donaldson, L., Vaidya, A., 2017. Visualising recalcitrance by colocalisation of
566 cellulase, lignin and cellulose in pretreated pine biomass using fluorescence
567 microscopy. Sci. Rep., 7, 44386.
568 12. Donohoe, B.S., Vinzant, T.B., Elander, R.T., Pallapolu, V.R., Lee, Y.Y., Garlock,
569 R.J., Balan, V., Dale, B.E., Kim, Y., Mosier, N.S., Ladisch, M.R., Falls, M., Holtzapple,
570 M.T., Sierra-Ramirez, R., Shi, J., Ebrik, M.A., Redmond, T., Yang, B., Wyman, C.E.,

571 Hames, B., Thomas, S., Warner, R.E., 2011. Surface and ultrastructural characterization
572 of raw and pretreated switchgrass. Bioresour. Technol., 102(24), 11097-11104.
573 13. dos Santos, A.C., Ximenes, E., Kim, Y., Ladisch, M.R. 2019. Lignin–Enzyme
574 Interactions in the Hydrolysis of Lignocellulosic Biomass. Trends Biotechnol., 37(5),
575 518-531.
576 14. El Hage, F., Legland, D., Borrega, N., Jacquemot, M.P., Griveau, Y., Coursol, S.,
577 Mechin, V., Reymond, M., 2018. Tissue Lignification, Cell Wall p-Coumaroylation and
578 Degradability of Maize Stems Depend on Water Status. J. Agric. Food Chem., 66(19),
579 4800-4808.
580 15. El Hage, F., Virlouvet, L., Lopez-Marnet, P.-L., Griveau, Y., Jacquemot, M.-P.,
581 Coursol, S., Méchin, V., Reymond, M., 2021. Responses of Maize Internode to Water
582 Deficit Are Different at the Biochemical and Histological Levels. Front. Plant Sci.,
583 12(167).
584 16. Fan, S., Zhang, P., Li, F., Jin, S., Wang, S., Zhou, S., 2016. A Review of
585 Lignocellulose Change During Hydrothermal Pretreatment for Bioenergy Production.
586 Curr. Org. Chem., 20(26), 2799-2809.
587 17. FAOSTAT. URL https://www.fao.org/faostat/fr/#data/ (accessed 22.03.25)
588 18. Gierlinger, N., Goswami, L., Schmidt, M., Burgert, I., Coutand, C., Rogge, T.,
589 Schwanninger, M., 2008. In Situ FT-IR Microscopic Study on Enzymatic Treatment of
590 Poplar Wood Cross-Sections. Biomacromolecules, 9(8), 2194-2201.
591 19. Gorzsás, A., Stenlund, H., Persson, P., Trygg, J., Sundberg, B., 2011. Cell-specific
592 chemotyping and multivariate imaging by combined FT-IR microspectroscopy and
593 orthogonal projections to latent structures (OPLS) analysis reveals the chemical
594 landscape of secondary xylem. Plant J., 66(5), 903-914.

595 20. Grabber, J.H., Hatfield, R.D., Ralph, J., 1998. Diferulate cross-links impede the
596 enzymatic degradation of non-lignified maize walls. J. Sci. Food Agric., 77(2), 193-200.
597 21. Herbaut, M., Zoghlami, A., Habrant, A., Falourd, X., Foucat, L., Chabbert, B., Paës,
598 G., 2018a. Multimodal analysis of pretreated biomass species highlights generic
599 markers of lignocellulose recalcitrance. Biotechnol. Biofuels, 11, 52.
600 22. Herbaut, M., Zoghlami, A., Paës, G., 2018b. Dynamical assessment of fluorescent
601 probes mobility in poplar cell walls reveals nanopores govern saccharification.
602 Biotechnol. Biofuels, 11, 271-271.
603 23. Jung, H.G., Casler, M.D., 2006. Maize Stem Tissues: Impact of Development on
604 Cell Wall Degradability. Crop Sci., 46.
605 24. Lam, M.S.-J.W.Q., Martinez, Y., Barbier, O., Jauneau, A., Pichon, M., 2013. Maize
606 cell wall degradability, from whole plant to tissue level : different scales of
607 complexity. Maydica, 58, 103-110.
608 25. Lam, T.B.-T., Iiyama, K., Stone, B.A., 2003. Hot alkali-labile linkages in the walls
609 of the forage grass Phalaris aquatica and Lolium perenne and their relation to in vitro
610 wall digestibility. Phytochemistry, 64(2), 603-607.
611 26. Leroy, A., Falourd, X., Foucat, L., Méchin, V., Guillon, F., Paës, G., 2021.
612 Evaluating polymer interplay after hot water pretreatment to investigate maize stem
613 internode recalcitrance. Biotechnol. Biofuels, 14(1), 164.
614 27. Li, T., Liu, N., Ou, X., Zhao, X., Qi, F., Huang, J., Liu, D., 2018. Visualizing
615 cellulase adsorption and quantitatively determining cellulose accessibility with an
616 updated fungal cellulose-binding module-based fluorescent probe protein. Biotechnol.
617 Biofuels, 11(1), 105.

618 28. Li, X., Lu, J., Zhao, J., Qu, Y., 2014. Characteristics of corn stover pretreated with
619 liquid hot water and fed-batch semi-simultaneous saccharification and fermentation for
620 bioethanol production. PLoS One, 9(4), e95455.
621 29. Luterbacher, J.S., Moran-Mirabal, J.M., Burkholder, E.W., Walker, L.P., 2015.
622 Modeling enzymatic hydrolysis of lignocellulosic substrates using fluorescent confocal
623 microscopy II: Pretreated biomass. Biotechnol. Bioeng., 112(1), 32-42.
624 30. Meng, X., Ragauskas, A.J., 2014. Recent advances in understanding the role of
625 cellulose accessibility in enzymatic hydrolysis of lignocellulosic substrates. Curr. Opin.
626 Biotechnol., 27, 150-158.
627 31. Nagle, N.J., Donohoe, B.S., Wolfrum, E.J., Kuhn, E.M., Haas, T.J., Ray, A.E.,
628 Wendt, L.M., Delwiche, M.E., Weiss, N.D., Radtke, C., 2020. Chemical and Structural
629 Changes in Corn Stover After Ensiling: Influence on Bioconversion. Front. Bioeng.
630 Biotechnol., 8.
631 32. Paës, G., Habrant, A., Ossemond, J., Chabbert, B., 2017. Exploring accessibility of
632 pretreated poplar cell walls by measuring dynamics of fluorescent probes. Biotechnol.
633 Biofuels, 10(1), 15.
634 33. Robert, P., Marquis, M., Barron, C., Guillon, F., Saulnier, L., 2005. FT-IR
635 Investigation of Cell Wall Polysaccharides from Cereal Grains. Arabinoxylan Infrared
636 Assignment. J. Agric. Food Chem., 53(18), 7014-7018.
637 34. Ropartz, D., Bodet, P.-E., Przybylski, C., Gonnet, F., Daniel, R., Fer, M., Helbert,
638 W., Bertrand, D., Rogniaux, H., 2011. Performance evaluation on a wide set of matrix-
639 assisted laser desorption ionization matrices for the detection of oligosaccharides in a
640 high-throughput mass spectrometric screening of carbohydrate depolymerizing
641 enzymes. Rapid Commun. Mass Spectrom., 25(14), 2059-2070.

642 35. Scheller, H.V., Ulvskov, P., 2010. Hemicelluloses. Annu. Rev. Plant Biol., 61(1),
643 263-289.
644 36. Simmons, T.J., Mortimer, J.C., Bernardinelli, O.D., Pöppler, A.-C., Brown, S.P.,
645 deAzevedo, E.R., Dupree, R., Dupree, P., 2016. Folding of xylan onto cellulose fibrils
646 in plant cell walls revealed by solid-state NMR. Nat. Commun., 7(1), 13902.
647 37. Siqueira, G., Milagres, A.M.F., Carvalho, W., Koch, G., Ferraz, A., 2011.
648 Topochemical distribution of lignin and hydroxycinnamic acids in sugar-cane cell walls
649 and its correlation with the enzymatic hydrolysis of polysaccharides. Biotechnol.
650 Biofuels, 4(1), 7.
651 38. Veličković, D., Ropartz, D., Guillon, F., Saulnier, L., Rogniaux, H., 2014. New
652 insights into the structural and spatial variability of cell-wall polysaccharides during
653 wheat grain development, as revealed through MALDI mass spectrometry imaging. J.
654 Exp. Bot., 65(8), 2079-2091.
655 39. Vermerris, W., Thompson, K.J., McIntyre, L.M., 2002. The maize Brown midrib1
656 locus affects cell wall composition and plant development in a dose-dependent manner.
657 Heredity, 88(6), 450-457.
658 40. Vidot, K., Devaux, M.-F., Alvarado, C., Guyot, S., Jamme, F., Gaillard, C., Siret,
659 R., Lahaye, M., 2019. Phenolic distribution in apple epidermal and outer cortex tissue
660 by multispectral deep-UV autofluorescence cryo-imaging. Plant Sci., 283, 51-59.
661 41. Vo, L.T.T., Girones, J., Jacquemot, M.-P., Legée, F., Cézard, L., Lapierre, C., Hage,
662 F.E., Méchin, V., Reymond, M., Navard, P., 2020. Correlations between genotype
663 biochemical characteristics and mechanical properties of maize stem - polyethylene
664 composites. Ind. Crops Prod., 143, 111925.

42. Wang, Q.Q., He, Z., Zhu, Z., Zhang, Y.-H.P., Ni, Y., Luo, X.L., Zhu, J.Y., 2012. Evaluations of cellulose accessibilities of lignocelluloses by solute exclusion and protein adsorption techniques. Biotechnol. Bioeng., 109(2), 381-389.

43. Wang, Y., Xu, X., Xue, H., Zhang, D., Li, G., 2021. Physical–chemical properties of cell wall interface significantly correlated to the complex recalcitrance of corn straw. Biotechnol. Biofuels, 14(1), 196.

44. Yang, Q., Pan, X., 2016. Correlation between lignin physicochemical properties and inhibition to enzymatic hydrolysis of cellulose. Biotechnol. Bioeng., 113(6), 1213-1224.

45. Yoo, C.G., Meng, X., Pu, Y., Ragauskas, A.J., 2020. The critical role of lignin in lignocellulosic biomass conversion and recent pretreatment strategies: A comprehensive review. Bioresour. Technol., 301, 122784.

46. Zeng, M., Ximenes, E., Ladisch, M.R., Mosier, N.S., Vermerris, W., Huang, C.-P., Sherman, D.M., 2012. Tissue-specific biomass recalcitrance in corn stover pretreated with liquid hot-water: Enzymatic hydrolysis (part 1). Biotechnol. Bioeng., 109(2), 390-397.

47. Zhao, X., Zhang, L., Liu, D., 2012. Biomass recalcitrance. Part I: the chemical compositions and physical structures affecting the enzymatic hydrolysis of lignocellulose. Biofuels Bioprod. Biorefining, 6(4), 465-482.

48. Zoghlami, A., Paës, G., 2019. Lignocellulosic Biomass: Understanding Recalcitrance and Predicting Hydrolysis. Front. Chem., 7(874).

687 **Figure captions**

688 **Fig. 1:** FASGA staining of (A) raw and (B) pretreated samples. Average spectra of raw
689 parenchyma (C) and of pretreated (D) rind parenchyma (RP) and of both pith
690 parenchyma (PP1 and PP2).

691 **Fig. 2:** Real-time monitoring of FTIR spectra, expressed as the sum of the absorbance
692 during enzymatic hydrolysis of (A) raw and of (B) pretreated (red) parenchyma near the
693 (red) rind (RP) and (blue) pith parenchyma (PP).

694 **Fig. 3:** Distribution and peak intensities of cellulose degradation products during
695 enzymatic hydrolysis revealed by MALDI-MS imaging. COS2 distribution (A; D) and
696 variations in the distribution of COSs according to the kinetics (B, E) in raw and
697 pretreated samples. The COS intensities detected during hydrolysis in (C) raw and (F)
698 pretreated samples. The white scale corresponds to 5 mm.

699 **Fig. 4:** Examples of time-lapse fluorescence images during enzymatic hydrolysis of (A)
700 raw RP and (B) HWP RP, and the changes over time in the enzymes fluorescence
701 intensity on the cell wall (C) and inside the lumen (D) under enzyme (Enz) and non-
702 enzyme (Buf) conditions. Blue signal corresponds to cell wall alone; Yellow, enzymes
703 alone; White, co-location of enzymes and cell walls. Field of view: $1{,}116 \times 1{,}116\ \mu m^2$.

704 **Fig. 5:** Examples of time-lapse fluorescence images during enzymatic hydrolysis of (A)
705 raw PP and (B) HWP PP, and changes in enzyme fluorescence intensity on the cell wall
706 (C) and inside the lumen (D) over time. The blue signal corresponds to cell wall alone;
707 Yellow, enzymes alone; White, co-location of enzymes and cell walls. The field of
708 view: $1{,}116 \times 1{,}116\ \mu m^2$.

709 **Fig. 6**: Analysis of variance of fluctuations in enzyme fluorescence measured in the
710 lumens. (A) before 15 min of hydrolysis; (B) after 80 min of enzymatic hydrolysis. Rrp

711 and Prp stand for Raw-RP and Pretreated-RP, respectively. Rpp and Ppp stand for Raw-
712 PP and Pretreated-PP, respectively.

713 **Table 1**: Diffusion coefficient of the DR40 measured in raw (RP) and HWP (PP). The
714 results are expressed as means of 3 to 5 repetitions, following the conditions, with
715 standard deviations in brackets. Different letters in the columns indicate significant
716 differences (T-test, $P<0.05$).

Fig. 1

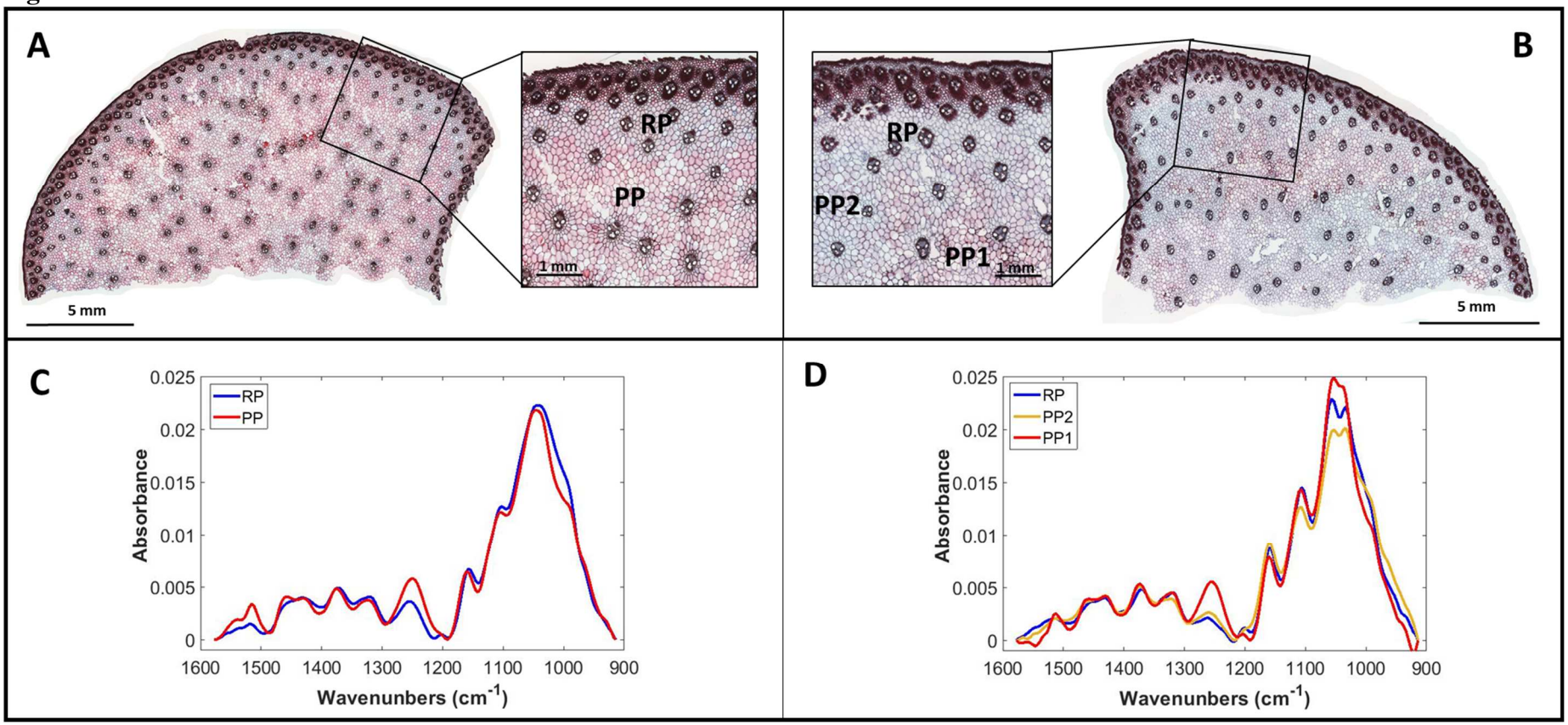
A
RP
PP
1 mm
5 mm
B
RP
PP2
PP1
1 mm
5 mm
C
RP
PP
Absorbance
Wavenunbers (cm-1)
D
RP
PP2
PP1
Absorbance
Wavenunbers (cm-1)

Fig. 2

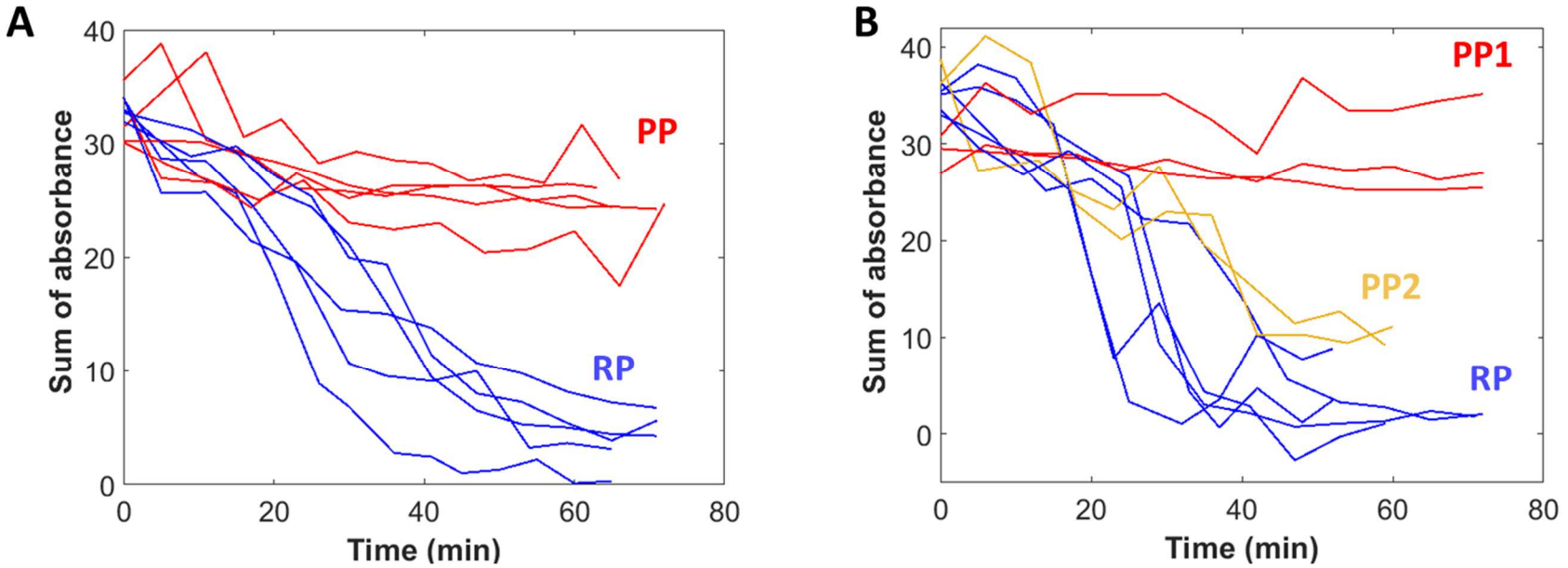
A
Sum of absorbance
Time (min)
PP
RP
B
Sum of absorbance
Time (min)
PP1
PP2
RP

Fig. 3

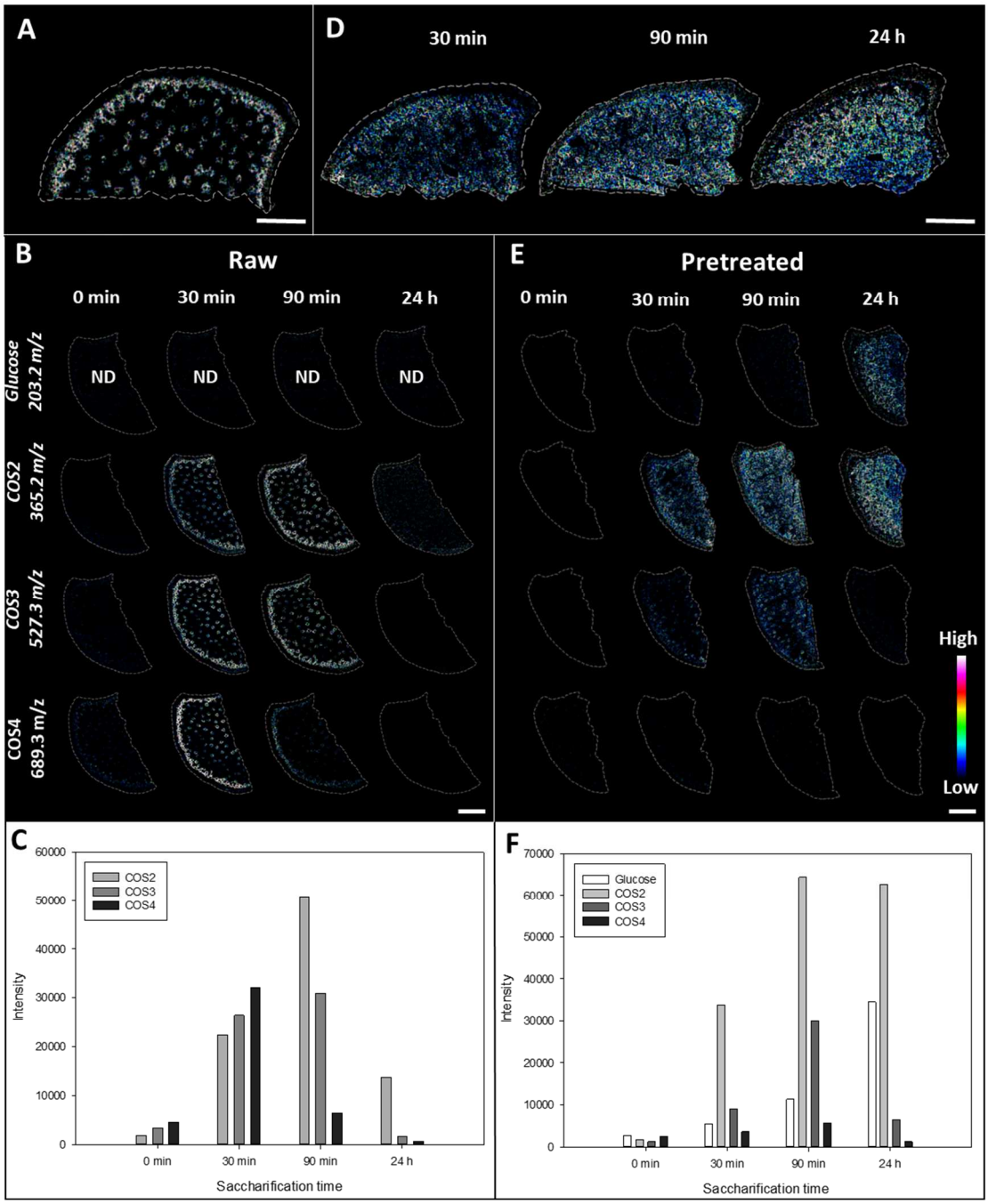
A
D
30 min
90 min
24 h
B
Raw
0 min
30 min
90 min
24 h
Glucose 203.2 m/z
COS2 365.2 m/z
COS3 527.3 m/z
COS4 689.3 m/z
ND
E
Pretreated
High
Low
C
COS2
COS3
COS4
Intensity
Saccharification time
F
Glucose
COS2
COS3
COS4
Intensity
Saccharification time

Fig. 4

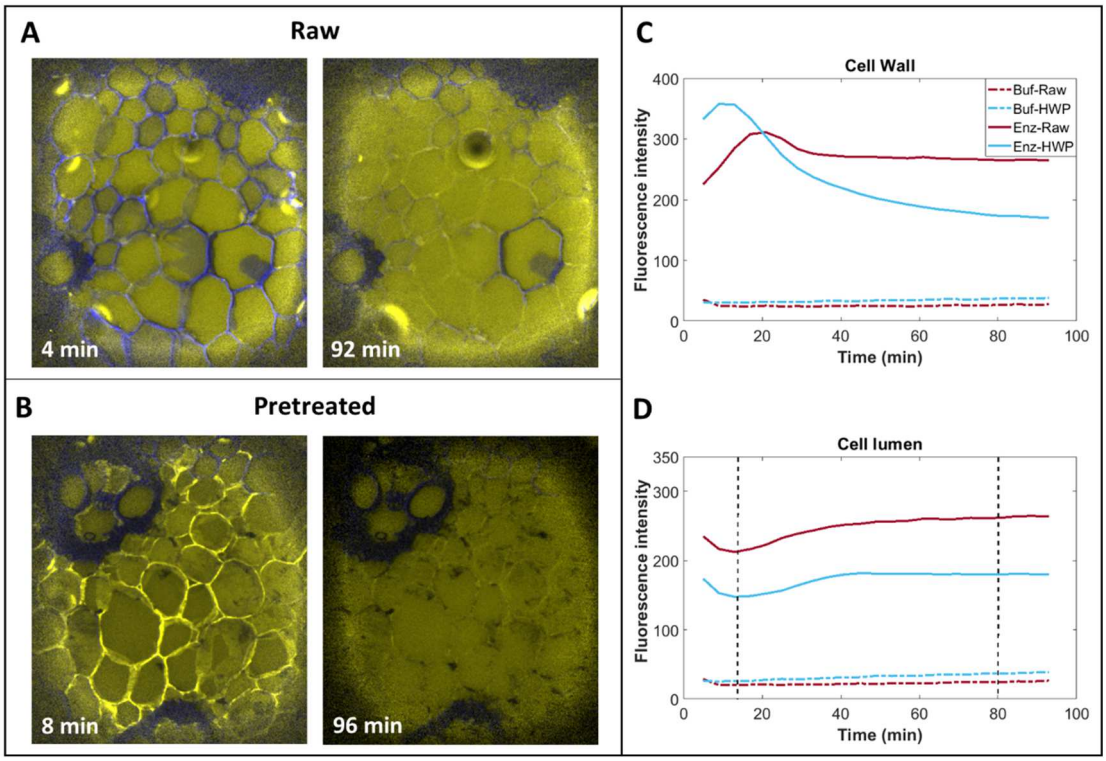
A
Raw
4 min
92 min
B
Pretreated
8 min
96 min
C
Cell Wall
Buf-Raw
Buf-HWP
Enz-Raw
Enz-HWP
Fluorescence intensity
Time (min)
D
Cell lumen
Fluorescence intensity
Time (min)

Fig. 5

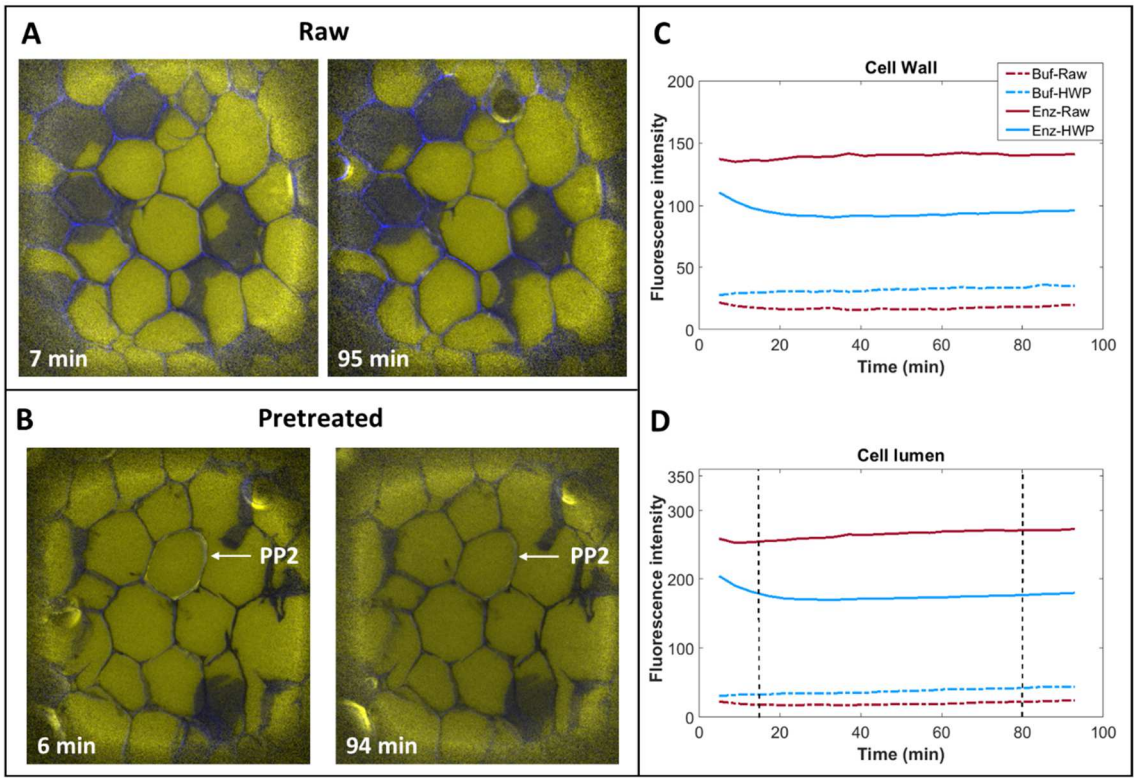
A
Raw
7 min
95 min
B
Pretreated
PP2
PP2
6 min
94 min
C
Cell Wall
Buf-Raw
Buf-HWP
Enz-Raw
Enz-HWP
Fluorescence intensity
Time (min)
D
Cell lumen
Fluorescence intensity
Time (min)

Fig. 6

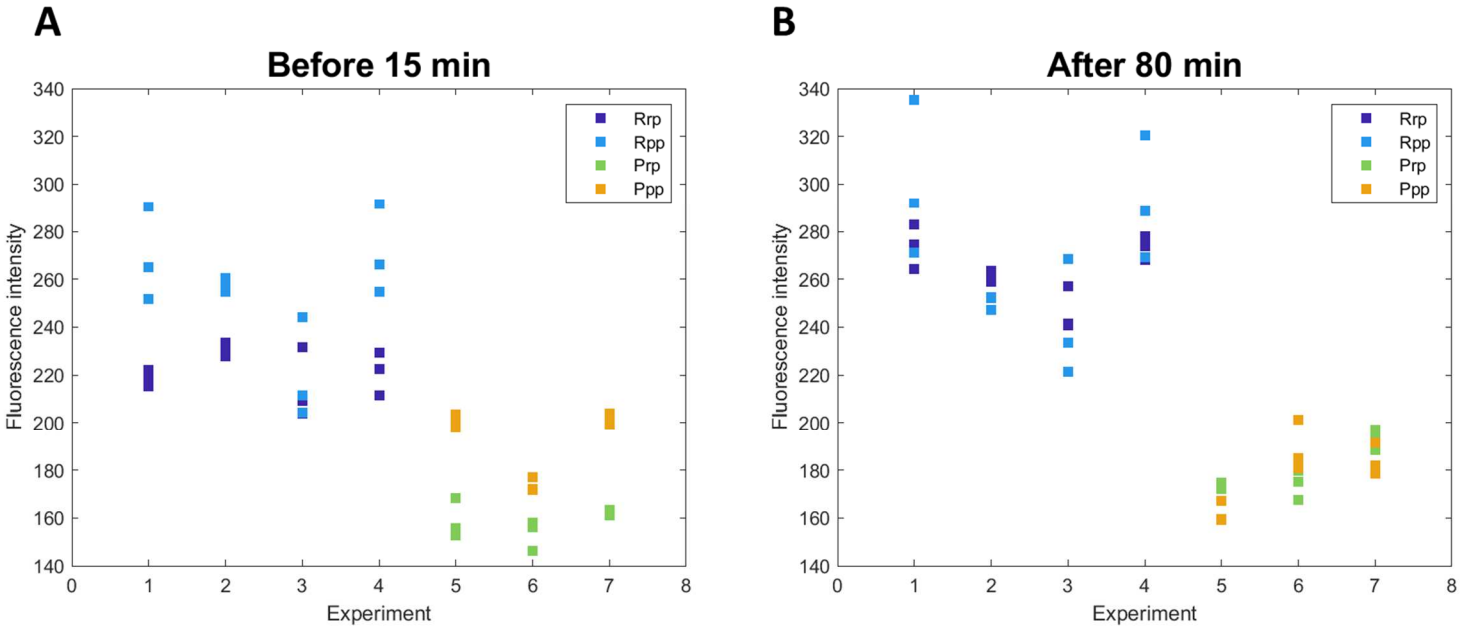

	Before 15 min		After 80 min	
	F-value	Prob > F	F-value	Prob > F
A- Pretreatment	149.71	0	179.58	0
B- Cell type	42.09	0	0.16	0.69
AB	0.01	0.942	0.53	0.47

Table 1:

	Raw		HWP		
	RP	PP	RP	PP1	PP2
Diffusion coefficient ($x10^{-2}.\mu m^2.s^{-1}$)	1.79 [a] (± 0.35)	1.13 [a] (± 0.13)	1.49 (± 0.33)	0.79 [b] (± 0.4)	1.44 [b] (± 0.2)

Chemical composition?

FASGA staining

Infrared

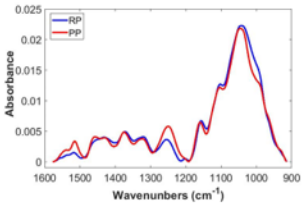

Localisation/mobility of the enzymes?

Enzyme autofluorescence

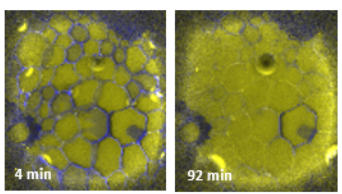

FRAP

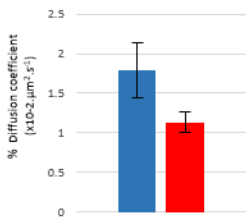

Raw and Hot water pretreated Maize internode

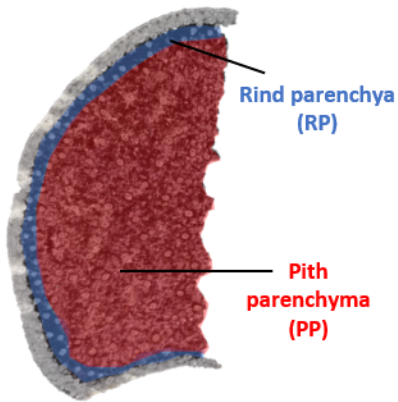

Enzymatic degradation efficiency?

Real-time monitoring by Infrared

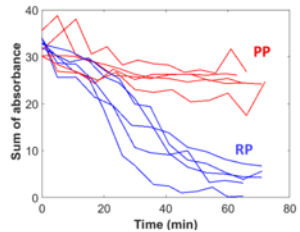

MALDI-MS imaging